

# Bio-Inspired Origami Metamaterials With Metastable Phases Through Mechanical Phase Transitions

Ke Liu

Department of Mechanical and Civil Engineering,  
California Institute of Technology,  
Pasadena, CA 91125  
e-mail: liuke@caltech.edu

Tomohiro Tachi

Department of General Systems Studies,  
School of Arts and Sciences,  
University of Tokyo,  
Tokyo 153-8902, Japan  
e-mail: tachi@idea.c.u-tokyo.ac.jp

Glaucio H. Paulino<sup>1</sup>

School of Civil and Environmental Engineering,  
Georgia Institute of Technology,  
Atlanta, GA 30332  
e-mail: paulino@gatech.edu

*Structural instability, once a catastrophic phenomenon to be avoided in engineering applications, is being harnessed to improve functionality of structures and materials, and has been a catalyst of substantial research in the field. One important application is to create functional metamaterials that deform their internal structure to adjust performance, resembling phase transformations in natural materials. In this paper, we propose a novel origami pattern, named the Shrimp pattern, with application to multi-phase architected metamaterials whose phase transition is achieved mechanically by snap-through. The Shrimp pattern consists of units that can be easily tessellated in two dimensions, either periodically with homogeneous local geometry or non-periodically with heterogeneous local geometries. We can use a few design parameters to program the unit cell to become either monostable or tune the energy barrier between the bistable states. By tessellating these unit cells into an architected metamaterial, we can create complex yet navigable energy landscapes, leading to multiple metastable phases of the material. As each phase has different geometries, the metamaterial can switch between different mechanical properties and shapes. The geometric origin of the multi-stable behavior implies that, conceptually, our designs are scale-independent, making them candidates for a variety of innovative applications, including reprogrammable materials, reconfigurable acoustic waveguides, and microelectronic mechanical systems and energy storage systems. [DOI: 10.1115/1.4050556]*

*Keywords:* elasticity, mechanical properties of materials, structures, origami, metamaterials

## 1 Introduction

Elastic structures with two or more possible equilibria can transition from one state to another via a rapid process known as snap-through. Snap-through allows plants and animals to store elastic energy and release it suddenly to generate rapid and powerful motions. Through a suite of structural modifications of their raptorial appendages, mantis shrimps generate forceful predatory strikes in a fraction of a second, which is so fast that it causes cavitation in the water [1,2]. Venus flytraps snap their leaves together rapidly to capture insects, which is enabled by the doubly curved geometry of the leaves [3]. Ladybird beetles fold their wings in a non-rigid foldable origami pattern to store elastic energy when stowed, which allows quick release of their wings when they start flying [4]. Similarly, the earwig wings have incompatible folding patterns, which remain open by a bistable locking mechanism during flight and self-fold rapidly without muscular actuation [5].

Such multi-stable structures, if adopted as building blocks of architected materials, can lead to some interesting and unprecedented properties beyond conventional materials [6–9], such as energy trapping [10,11], elastic pattern formation [12,13], and guided transition waves [14]. In this work, we aim to design an architected material that can switch properties by multi-stable snapping [15–18], resembling the concept of phase transitions. Owing to the different structures at the atomic and molecular scale, the same material displays different properties in different phases. For natural

materials, the transitions between phases are characterized by changes in thermodynamic states. The concept of a phase being a rearranged structural form of materials can be generalized at larger scales, which results in architected materials whose internal structures can be intentionally changed to display different properties on demand.

As suggested by examples found in nature [3–5], origami patterns can organize geometry of thin sheets and membranes to produce functionality by harnessing their inherent elastic instabilities [19–23]. There are a few known origami patterns that lead to structures with multi-stability. Examples include the square twist [24], the Kresling tube [25], and the hypar origami [26]. However, many of these patterns cannot be easily tessellated due to irregular geometry (e.g., Kresling tube), or if they can be tessellated, their deformation modes and multi-stable energy landscape differ significantly between the unit cell and tessellation, making their behavior difficult to predict (e.g., the square twist [24] and hypar origami pattern [26]).

In this paper, we present a multi-stable origami pattern, named the Shrimp pattern (see Fig. 2), whose geometry is tailored to accommodate tessellations easily. The pattern is inspired by the segmented structure of the shrimp, and hence named after it, as shown in Fig. 1. The Shrimp pattern combines features of both rigid and non-rigid origami, allowing the pattern to behave as a rigid origami [27] in a range of stable configurations, while the switching between different ranges of stable configurations has to go through an energy barrier by snap-through (i.e., non-rigid origami) [28]. The bistability of a unit cell of this pattern can be programmed by a few geometric parameters. Hence, if used for architected materials, the Shrimp tessellated material would have multiple stable phases, and switch between phases is possible through snap-through, which is interpreted as mechanical phase transition. We further show that the Shrimp tessellated material exhibits different

<sup>1</sup>Corresponding author.

Contributed by the Applied Mechanics Division of ASME for publication in the JOURNAL OF APPLIED MECHANICS. Manuscript received December 10, 2020; final manuscript received February 2, 2021; published online May 14, 2021. Tech. Editor: Yonggang Huang.



**Fig. 1** Various stable states of a multi-stable Shrimp pattern tessellation, which has a segmented structure similar to arthropods such as shrimps. This curved design is a generalization from the standard Shrimp pattern, whose geometry is elaborated upon in Appendix A.

mechanical properties in its different phases. Moreover, because each Shrimp unit cell is bistable, by tessellating the Shrimp unit cells, the number of phases of the resultant architected material grows combinatorially.

The remainder of the article is organized as follows. Section 2 describes the geometry of the standard Shrimp pattern unit that tessellates on a plane. Section 3 explains how the energy landscape of a single Shrimp unit cell can be programed. Section 4 verifies the programable bistable behavior by means of a reduced-order bar-and-hinge numerical model. Section 5 elaborates on the creation of the multi-stable architected material by tessellating the Shrimp unit cells. More importantly, we demonstrate that the Shrimp tessellated material can switch property by mechanical phase transition. We summarize current work and propose future development in Sec. 6. Appendix A explains the strategy to tessellate the Shrimp pattern in curved configuration. Appendix B supplements the paper by offering tips for fabricating the non-developable Shrimp pattern.

## 2 Geometry of the Standard Shrimp Unit

The geometry of a standard Shrimp pattern unit is described in Fig. 2. The length parameters include panel width  $a$ , front panel length  $b$ , rear panel length  $c$ , and tail length  $d$ . The angular parameters include front panel angle  $\alpha_F$ , rear panel angle  $\alpha_R$ , and rib (tri-angle) panel angle  $\alpha_B$ . For standard Shrimp pattern designs, edge length  $c$  satisfies the following condition:

$$c = \frac{a \cos \alpha_F}{\cos \alpha_R} \quad (1)$$

The edges of length  $a$  lie in the  $xz$ -plane, as shown in Fig. 2.

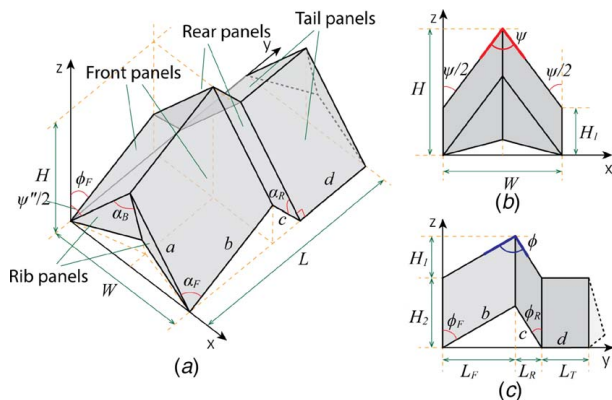


**Fig. 2** Geometry of a shrimp unit cell: (a) isometric view, (b) and (c) side views

Although within each unit cell the tail panels are not connected to the rib panels, in an assembly/tessellation of the Shrimp pattern, the rib panels are actually between the tail panels and front panels, and they should be attached to the last row of tail panels.

When  $\psi \leq 2\alpha_B$ , the Shrimp pattern allows rigid origami behavior with a single degree-of-freedom (DOF). The configuration is determined by any of the three edge inclination angles ( $\psi/2$ ) ( $=\psi_2$ ),  $\phi_F$ , and  $\phi_R$ , which are related as follows:

$$\cos(\psi/2) \cos \phi_F = \cos \alpha_F \quad (2)$$

$$\cos(\psi/2) \cos \phi_R = \cos \alpha_R \quad (3)$$

We define the shaping angles of the Shrimp pattern by

$$\phi = \phi_F + \phi_R \quad (4)$$

$$\psi = \psi' = \psi'' \quad (5)$$

Accordingly, the heights ( $H, H_1, H_2$ ), width ( $W$ ), and lengths ( $L, L_1, L_2, L_3$ ) of the Shrimp unit cell are given by

$$H_1 = b \cos \phi_F = c \cos \phi_R \quad (6)$$

$$H_2 = a \cos(\psi/2) \quad (7)$$

$$H = H_1 + H_2 \quad (8)$$

$$W = 2a \sin(\psi/2) \quad (9)$$

$$L_F = b \sin \phi_F \quad (10)$$

$$L_R = c \sin \phi_R \quad (11)$$

$$L_T = d \quad (12)$$

$$L = L_F + L_R + L_T \quad (13)$$

To understand the folding of the Shrimp origami, it is also important to calculate the dihedral folding angles labeled in Fig. 3. We can derive that, when  $\psi \leq 2\alpha_B$ ,

$$\gamma_{FR} = \sin^{-1} \left( \frac{\sin \phi_F}{\sin \alpha_F} \right) + \sin^{-1} \left( \frac{\sin \phi_R}{\sin \alpha_R} \right) \quad (14)$$

$$\gamma_{FF} = 2 \sin^{-1} \left( \frac{\sin(\psi/2)}{\sin \alpha_F} \right) \quad (15)$$

$$\gamma_{RR} = 2 \sin^{-1} \left( \frac{\sin(\psi/2)}{\sin \alpha_R} \right) \quad (16)$$

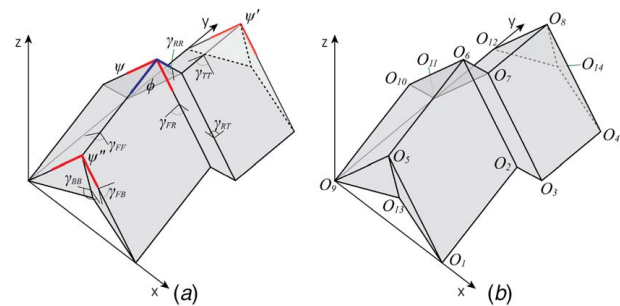


**Fig. 3** Labels of geometric quantities of a shrimp unit cell: (a) dihedral folding angles and (b) vertices

$$\gamma_{RT} = \frac{\pi}{2} + \sin^{-1} \left( \frac{\sin \phi_R}{\sin \alpha_R} \right) \quad (17)$$

$$\gamma_{TT} = \psi' = \psi = \psi'' \quad (18)$$

$$\gamma_{FB} = \pi - \sin^{-1} \left( \frac{\sin \phi_F}{\sin \alpha_F} \right) - \cos^{-1} \left( \frac{\tan(\psi/2)}{\tan \alpha_B} \right) \quad (19)$$

$$\gamma_{BB} = 2 \sin^{-1} \left( \frac{\sin(\psi/2)}{\sin \alpha_B} \right) \quad (20)$$

Based on the above geometric relations, we can analytically derive the Poisson's ratio of the shrimp pattern, which is given by

$$\begin{aligned} \nu_{yx} &= -\frac{dL/L}{dW/W} = -\frac{dL/d\psi}{dW/d\psi} \left( \frac{W}{L} \right) \\ &= \frac{\tan^2(\psi/2)}{L \cos(\psi/2)} \left( \frac{b \cos^2 \alpha_F}{\sqrt{\cos^2(\psi/2) - \cos^2 \alpha_F}} \right. \\ &\quad \left. \pm \frac{c \cos^2 \alpha_R}{\sqrt{\cos^2(\psi/2) - \cos^2 \alpha_R}} \right) \end{aligned} \quad (21)$$

The “ $\pm$ ” sign in Eq. (21) depends on whether crease  $O_6 O_7$  is a mountain or valley fold. When  $O_6 O_7$  is a mountain fold, the Shrimp pattern is said to be in its eggbox mode ( $E$ ), and the “+” sign shall be used in Eq. (21). When  $O_6 O_7$  is a valley fold, the Shrimp pattern is said to be in its Miura mode ( $M$ ), and the “-” sign shall be used. This feature is inherited from the Morph pattern investigated in Ref. [29], as the Shrimp pattern shares the same geometry with the Morph pattern by deleting the tail and rib panels. Figure 4 shows how the geometric parameters (a)  $\alpha_F$ , (b)  $\alpha_R$ , (c)  $d$ , and (d)  $b/a$  affect the Poisson's ratio of a Shrimp unit. We note that in the limit of  $d=0$ , the value of  $\nu_{yx}$  recovers that of the Morph pattern [29]. The above derivation only applies to the

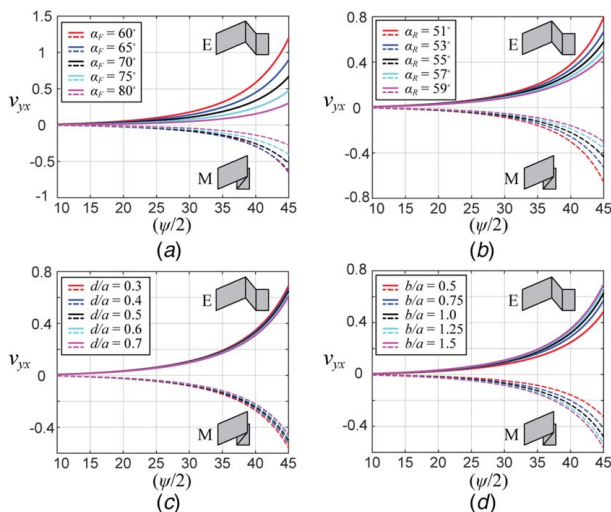


**Fig. 4** Poisson's ratio ( $\nu_{yx}$ ) of shrimp unit cells with different geometries at various folding states characterized by  $(\psi/2)$ . We examine the effect on Poisson's ratio of four geometric parameters. (a) The front panel angle  $\alpha_F$ , with  $a = 20$ ,  $b = 25$ ,  $d = 10$ ,  $\beta_0 = 45$  deg,  $\alpha_R = 53$  deg. (b) The rear panel angle  $\alpha_R$ , with  $a = 20$ ,  $b = 25$ ,  $d = 10$ ,  $\beta_0 = 45$  deg,  $\alpha_F = 70$  deg. (c) The relative tail length  $d/a$ , with  $a = 20$ ,  $b = 25$ ,  $\beta_0 = 45$  deg,  $\alpha_F = 70$  deg,  $\alpha_R = 53$  deg. (d) Front panel length to width ratio  $b/a$ . For each case, the parameter values are given in the plots. Moreover,  $M$  denotes the Miura mode and  $E$  denotes the eggbox mode.

rigid origami range of the Shrimp pattern, when the folding process is periodic across all unit cells. However, in reality, due to the compliance of the panels, a true rigid origami behavior is rarely observed [28].

### 3 Creating Bistability by Breaking Connectedness of Configuration Space

According to Ref. [30], when different stable configurations of a multi-stable origami are not connected by any continuous rigid origami kinematic path, the origami is said to be topologically bistable, as its configuration space of rigid origami kinematics is disconnected. When there is no rib panel attached, the shaping angles  $\phi$  and  $\psi$  ( $= \psi' = \psi''$ ) are related by the following formula:

$$\cos \psi = \cos 2\alpha_F + \frac{2(\cos \alpha_R - \cos \alpha_F \cos \phi)^2}{\sin^2 \phi} \quad (22)$$

which is plotted in Fig. 5, in terms of  $\psi'$  and  $\phi$ .

However, owing to the existence of rib panels,  $\psi'$  and  $\psi''$  cannot exceed  $2\alpha_B$ , and thus a certain range of folding is blocked under rigid origami assumption, as indicated by the dashed lines in Fig. 5. The solid parts of the curves refer to the remaining rigidly foldable ranges of the Shrimp pattern, which is separated into two disconnected parts. The two limit configurations of the blocked range of rigid folding (dashed lines in Fig. 5) in terms of  $\phi$  are given by

$$\phi = \cos^{-1} \left( \frac{\cos \alpha_F}{\cos \alpha_B} \right) \pm \cos^{-1} \left( \frac{\cos \alpha_R}{\cos \alpha_B} \right) \quad (23)$$

We denote the difference between the two limit configurations as  $\Delta\phi$

$$\Delta\phi = 2 \cos^{-1} \left( \frac{\cos \alpha_R}{\cos \alpha_B} \right) \quad (24)$$

which becomes independent from  $\alpha_F$ .

In reality, the compliance of materials offers extra DOF that allow the Shrimp pattern to transition between the two disconnected rigid origami configurational ranges through non-rigid deformation. The tail panels are added to allow the blocked range to be overcome by gentle panel bending; otherwise, the blocked range of rigid folding can only be overcome by stretching the materials, which is likely to generate rupture or other types of irreversible damages. Together, the addition of rib panels and tail panels leads to bistable snapping between the two disconnected parts of the rigid origami configurations of the Shrimp pattern. The conditions for the emergence of bistability are discussed later.

As illustrated in Fig. 6(a), the folding energy of the system increases as the pattern is folded away from the initial configuration, but the bending energy only appears within the blocked range of rigid folding, i.e., when  $\psi > 2\alpha_B$ . While the bending energy

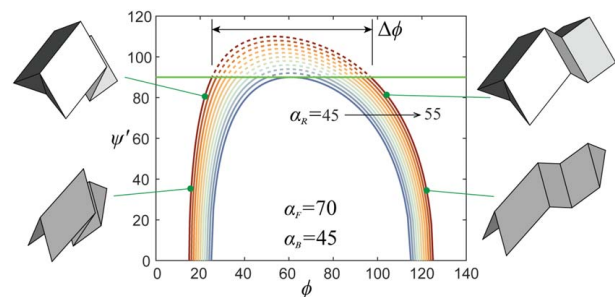


**Fig. 5** Configuration space of the Shrimp pattern in terms of  $\psi'$  and  $\phi$ . The dashed portion of the curves cannot be reached kinematically under the assumption of rigid origami.

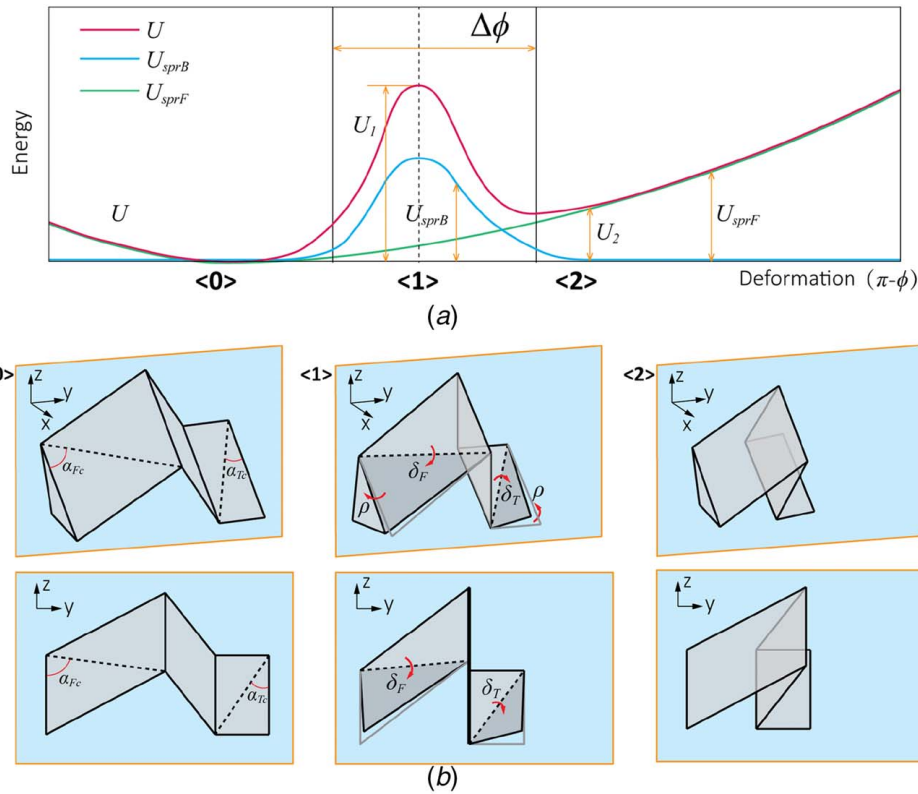


**Fig. 6** A hypothetical deformation process of a shrimp unit cell and the associated energy states of the system. (a) The change of system energy ( $U$ ) for a deformed Shrimp pattern, as a summation of bending ( $U_{sprB}$ ) and folding energy ( $U_{sprF}$ ), with respect to the deformation measured by  $\pi - \phi$ . Stretching deformation (and energy) are not considered by the isometric assumption. (b) The idealized configurations of a shrimp unit cell during its deformation. Configuration  $\langle 0 \rangle$ : the initial configuration. Configuration  $\langle 1 \rangle$ : the non-rigid deformed configuration during snapping, when the bending energy in the system reaches maximum. Configuration  $\langle 2 \rangle$ : the after-snapping configuration—we can see that the rear and tail panels are mirror symmetric with respect to their initial configuration about the panel spanned by  $O_2$ ,  $O_6$ , and  $O_{10}$ .

gradually vanishes beyond the range of non-rigid folding, the folding energy keeps increasing. Therefore, if the stored energy becomes smaller than the peak energy after the non-rigid deformation, the Shrimp pattern will experience bistability. We denote the initial configuration as configuration 0, the peak energy state as configuration 1, and the state after non-rigid folding as configuration 2, i.e., the metastable state (see Fig. 6(b)).

### 3.1 Estimating Peak Energy During the Non-Rigid Folding Range.

Although the actual non-rigid deformation of the Shrimp pattern during the transitioning is a complex combination of bending, folding, and stretching, we may consider a simplified deformation process to estimate the peak energy by assuming isometric deformations. We assume that only the front and tail panels will bend along one of their diagonals, as demonstrated in Fig. 6(a). Therefore,  $\psi$  can be different from  $\psi'$  and  $\psi''$  and can exceed  $2\alpha_B$ , as depicted in Fig. 6(b)(0).

Due to symmetry about the middle plane, we can consider that both front panels (or tail panels) experience the same amount of bending. We denote the bending angle of the front panels as  $\delta_F$  and the bending angle of the tail panels as  $\delta_T$ . We define  $\rho$  as the rotation angle of edge  $O_1 O_2$  (see Fig. 6(b)(1)), which can be approximated by

$$\rho \approx \psi/2 - \alpha_B \quad (25)$$

when the bending of panels are small. At vertex  $O_5$ , using spherical trigonometry, we obtain

$$\cos \delta_F = \frac{\cos \rho - \cos^2 \alpha_{Fc}}{1 - \cos^2 \alpha_{Fc}} \quad (26)$$

where

$$\cos \alpha_{Fc} = \frac{a^2 - ab \cos \alpha_1}{a\sqrt{a^2 + b^2 - 2ab \cos \alpha_1}} \quad (27)$$

For the tail panels, at vertex  $O_8$ , we obtain

$$\cos \delta_T = \frac{\cos \rho - \cos^2 \alpha_{Tc}}{1 - \cos^2 \alpha_{Tc}} \quad (28)$$

where

$$\cos \alpha_{Tc} = \frac{a}{\sqrt{a^2 + d^2}} \quad (29)$$

We can see that  $\rho$  is largest when  $\psi = 2\alpha_R$ , and consequently,  $\delta_F$  and  $\delta_T$  become maximal. Therefore, the total bending energy reaches peak when  $\psi = 2\alpha_R$ , when the two rear panels become coplanar. According to Eqs. (26) and (28), the maximal bending angles are given by

$$\delta_{F, \max} = \cos^{-1} \left( \frac{\cos(\alpha_R - \alpha_B) - \cos^2 \alpha_{Fc}}{1 - \cos^2 \alpha_{Fc}} \right) \quad (30)$$

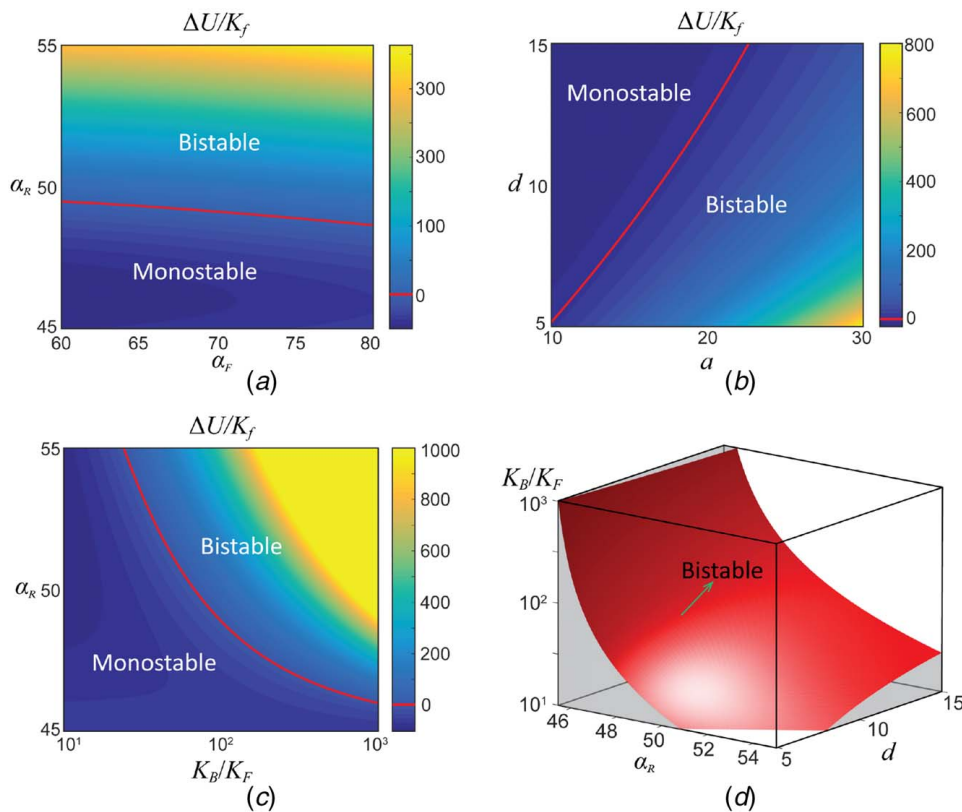


**Fig. 7 Programmable energy state of a shrimp unit cell. A positive energy difference  $\Delta U$  indicates that the pattern is bistable. (a)–(c) Show how  $\Delta U$  is affected by geometric parameters (i.e.,  $\alpha_F$ ,  $\alpha_R$ ,  $a$ ,  $d$ ) and material properties (i.e.,  $k_0^B/k_0^F$ ). In (d), we plot the limit surface of the emergence of bistability in the configuration space spanned by  $\alpha_R$ ,  $d$ ,  $k_0^B/k_0^F$ .**

$$\delta_{T, \max} = \cos^{-1} \left( \frac{\cos(\alpha_R - \alpha_B) - \cos^2 \alpha_{Tc}}{1 - \cos^2 \alpha_{Tc}} \right) \quad (31)$$

Hence, we obtain the peak bending energy as

$$U_{sprB,1} = k_0^B (\delta_{F, \max}^2 + \delta_{T, \max}^2) \quad (32)$$

where  $k_0^B$  denotes the linear bending stiffness. Assuming the initial configuration of the Shrimp origami structure is stress-free, the folding energy at  $\psi = 2\alpha_R$  is calculated as

$$\begin{aligned} U_{sprF,1} = & \frac{1}{2} k_0^F ((\gamma_{BB,1} - \gamma_{BB,0})^2 + 2(\gamma_{FB,1} - \gamma_{FB,0})^2 \\ & + (\gamma_{FF,1} - \gamma_{FF,0})^2 + 2(\gamma_{FR,1} - \gamma_{FR,0})^2 \\ & + (\gamma_{RR,1} - \gamma_{RR,0})^2 + 2(\gamma_{RT,1} - \gamma_{RT,0})^2 \\ & + (\gamma_{TT,1} - \gamma_{TT,0})^2) \end{aligned} \quad (33)$$

where the initial angles in Eq. (33) can be computed using Eqs. (14)–(20) given  $\psi_0$  and  $\phi_0$ . The symbol  $k_0^F$  denotes the linear folding stiffness. The deformed angles at configuration 1 can be estimated by taking  $\psi_1 = 2\alpha_R$  and  $\phi_{R,1} = 0$  using the same set of equations. The total energy at peak is a combination of folding and bending energy:

$$U_1 = U_{sprB,1} + U_{sprF,1} \quad (34)$$

Owing to the restricted kinematics, this estimated peak energy is likely to be greater than the actual peak.

**3.2 Estimating Stored Energy After Snapping.** Configuration 2 occurs when the rear panels are at symmetric positions

compared to the initial configuration (i.e., configuration 0), that is when

$$\psi_2 = \psi_0 \quad (35)$$

and

$$\phi_2 = \begin{cases} \phi_{F,0} - \phi_{R,0} & \text{if } \phi_0 = \phi_{F,0} + \phi_{R,0} \\ \phi_{F,0} + \phi_{R,0} & \text{if } \phi_0 = \phi_{F,0} - \phi_{R,0} \end{cases} \quad (36)$$

where

$$\begin{aligned} \phi_{F,0} &= \cos^{-1} \left( \frac{\cos \alpha_F}{\cos(\psi_0/2)} \right) \\ \phi_{R,0} &= \cos^{-1} \left( \frac{\cos \alpha_R}{\cos(\psi_0/2)} \right) \end{aligned} \quad (37)$$

At this configuration, only the angles of  $\gamma_{FR}$ ,  $\gamma_{RR}$ , and  $\gamma_{RT}$  experience deformation, and the other folding hinges stay at the same angles as in the initial configuration. The three dihedral angles can be derived based on Eqs. (35) and (36), using Eqs. (14)–(20). Then we can compute the stored energy at configuration 2 as

$$\begin{aligned} U_2 = U_{sprF,2} = & \frac{k_0^F}{2} [2(\gamma_{FR,2} - \gamma_{FR,0})^2 \\ & + (\gamma_{RR,2} - \gamma_{RR,0})^2 + 2(\gamma_{RT,2} - \gamma_{RT,0})^2] \end{aligned} \quad (38)$$

If it exists, the bistable state with locally minimal energy happens before the assumed configuration 2, thus Eq. (38) overestimates the minimal energy after the non-rigid folding. However, because Eq. (34) also overestimates the peak energy, when we use  $\Delta U = U_1 - U_2$  to determine the existence of a metastable state, the error shall be reduced.

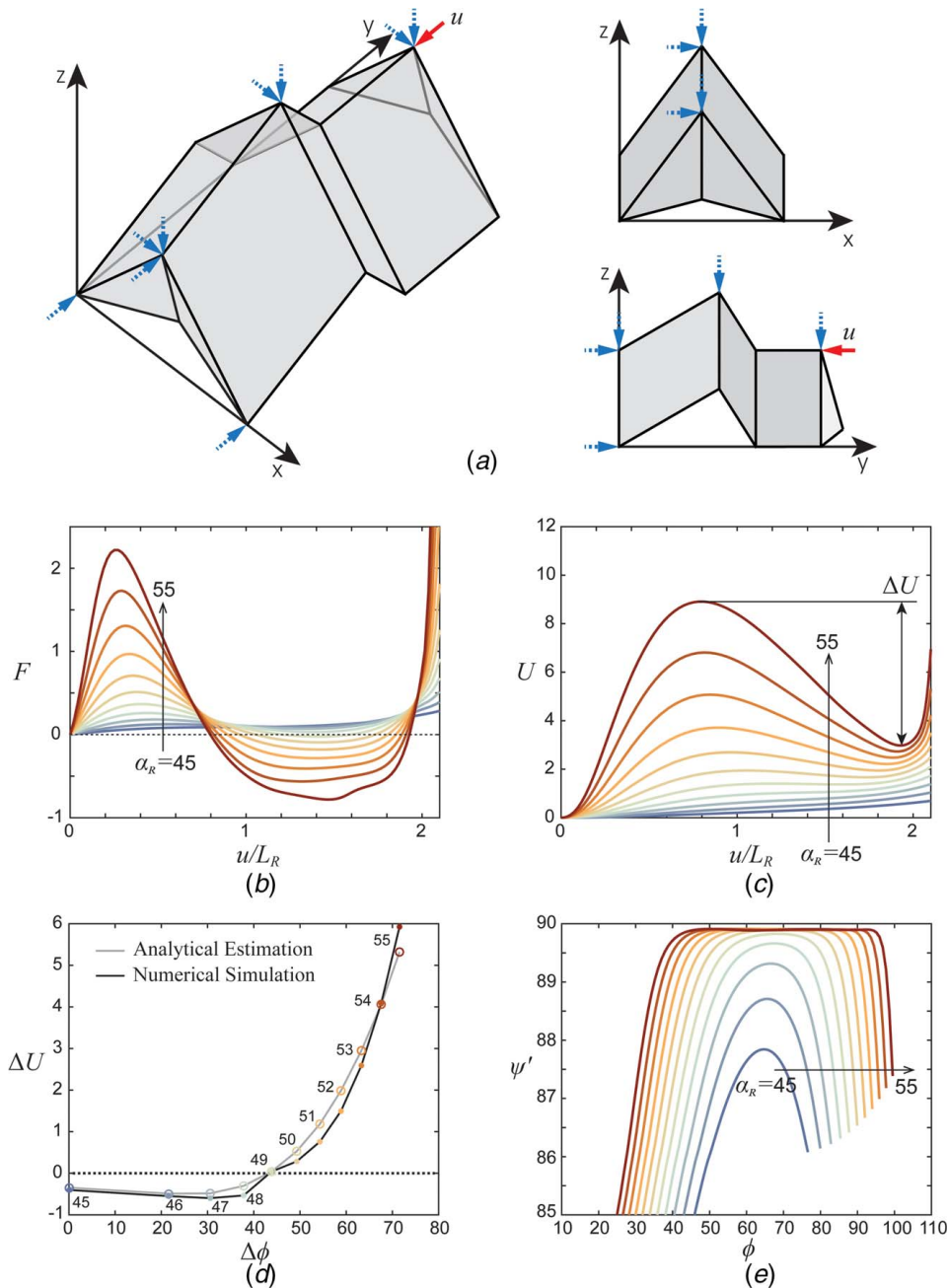


**Fig. 8 Numerical verification of the programmable energy landscape of shrimp unit cell. (a) Boundary conditions for the numerical simulation. Dashed arrows are fixed DOF, and the solid arrow refers to applied displacement  $u$ . (b) Force versus (normalized) displacement curve. The displacement  $u$  is normalized by  $L_R$  of each design. The behavior of a shrimp unit cell as  $\alpha_R$  varies from 45 deg to 55 deg. (c) The stored energy versus (normalized) displacement. (d) Comparison between the analytical estimation of  $\Delta U$  as formulated in Sec. 3 with the numerically obtained values. When the structure is monostable,  $\Delta U$  is taken as the difference between the stored energy at  $u/L_R = 1$  and  $u/L_R = 2$  for the numerical models. (e) The opening of angle  $\psi'$  during deformation. We see that  $\psi'$  is always smaller than  $2\alpha_B (= 90 \text{ deg})$ .**

**3.3 Determining Existence of Metastable State.** As illustrated in Fig. 6, if  $\Delta U = U_1 - U_2 > 0$ , a local minimum of stored energy exists besides the initial configuration (i.e., the metastable state), and thus the Shrimp pattern exhibits bistability. This energy difference is affected by the geometry of the pattern and material properties. Since we assume isometric deformations, according to Eqs. (34) and (38), the material-associated parameter that influences the value of  $\Delta U$  is  $k_0^B/k_0^F$ , the ratio between bending stiffness and folding stiffness.

Figures 7(a) and 7(b) show the variation of  $\Delta U$  with respect to the pairs of geometric parameters ( $\alpha_F$ ,  $\alpha_R$ ), and ( $a$ ,  $d$ ). We observe that  $\alpha_R$  and  $a$  have positive influence on  $\Delta U$ , while  $d$  has negative influence. We also find that  $\alpha_F$  does not have significant influence on  $\Delta U$ . The effect of  $k_0^B/k_0^F$  is plotted in Fig. 7(c) in pair with  $\alpha_R$ . The emergence of the bistability is defined by the contour of  $\Delta U = 0$ , which is plotted in Fig. 7(d) as a function of  $\alpha_R$ ,  $d$ , and  $k_0^B/k_0^F$ . When  $k_0^B/k_0^F$  is larger, the Shrimp pattern exhibits bistability over a wider range of geometries.

#### 4 Verifying Bistable Behavior by Numerical Simulations

To verify the analytical analysis about the bistable behavior of the Shrimp pattern unit cell, we conduct numerical simulations using the bar-and-hinge model. The implementation in this work is based on the N5B8 discretization scheme [31]. The basic idea of the N5B8 discretization is explained in Refs. [31,32]. We assume that Young's modulus  $E=1$  GPa, Poisson's ratio  $\nu=0.3$ , and sheet thickness  $t=0.5$  mm. The stiffness of folding hinges are assigned through scalable formulas as in Ref. [31]. We take the length scale factor  $L^*$  to be  $30L_F$ , relative to the length of each folding hinge, which yields an average ratio between bending and folding stiffness per length  $k_0^B/k_0^F \approx 80$ .

The results from numerical simulations of compressive folding are presented in Fig. 8. The boundary conditions for the numerical analysis are shown in Fig. 8(a). In this study, we fix some geometric parameters as  $\alpha_F = 70$  deg,  $d = 10$  mm,  $a = 20$  mm, and  $b = 25$  mm. When  $\alpha_R > 49$  deg, the bistable behavior starts to appear. The displacement  $u$  measures the movement of node  $O_8$  in the direction of loading (i.e.,  $-y$ ). We normalize the displacement  $u$  by  $L_2$ , such that (1) when  $u/L_2 = 1$ , the rear panels are approximately coplanar, close to configuration 1 in the analytical derivation and (2) when  $u/L_2 = 2$ , the rear panels snap inside the front panels, close to configuration 2 in the analytical derivation.

The negative forces in Fig. 8(b) during the bistable snapping display a long (negative) plateau without a strong peak, which behaves quite differently from most bistable origami structures, including the hyper origami [26]. The lack of strong negative peak force indicates that the snapping of the Shrimp pattern is a gentle process. We observe a stiffening effect occurring immediately after the snapping, as indicated by the sharp increase of forces when  $u/L_2 > 2$  in Fig. 8(b). As expected in the analytical analysis, if bistability appears, the stored energy of the Shrimp pattern experiences a peak near  $u/L_2 = 1$  and a local minimum around  $u/L_2 = 2$  (see Fig. 8(c)). As shown in Fig. 8(d), the analytical estimations of the energy difference  $\Delta U$  agree well the numerically computed energy barriers. We record the angles of  $\psi'$  during the simulations, as shown in Fig. 8(e). Compared with Fig. 5, we can clearly see that  $\psi'$  is kinematically constrained to be below  $2\alpha_B$  ( $= 90$  deg).

The numerical simulations verify that the energy landscape of the Shrimp pattern is programmable, through geometric variations of the rear panel angle  $\alpha_R$ . As  $\alpha_R$  increases, both the peak force and magnitude of energy barrier (i.e.,  $\Delta U$ ) increase accordingly. Such monotonic relationship allows for easy interpretation and manipulation of the mechanical properties of the Shrimp pattern.

#### 5 Metastable Phases and Phase Transition of the Shrimp Tessellated Material

The programmable bistability of the Shrimp pattern unit cell allows us to create architected materials with metastable phases by tessellating the shrimp unit cells. The compatibility condition for tessellation is that: in the  $x$ -direction, angle  $\psi'$  of one unit must match  $\psi''$  of the next unit; and in the  $y$ -direction, angle  $\phi$ , and tail length  $d$  of adjacent units must be equal. Figure 9(a) shows an example of such designs when we tessellate three shrimp units in the  $x$ -direction to form a chain.

The state of least energy (when  $U = 0$ ) of the Shrimp tessellation occurs when all three units are in their eggbox mode. Denote  $\psi_0$  as angle  $\psi$  at the state of least energy. We consider three variants of this tessellation: (1)  $\psi_0 = 66$  deg,  $\alpha_R = 53$  deg; (2)  $\psi_0 = 86$  deg,  $\alpha_R = 53$  deg; and (3)  $\psi_0 = 86$  deg,  $\alpha_{R,AB} = 55$  deg,  $\alpha_{R,BC} = 53$  deg, and  $\alpha_{R,CD} = 51$  deg; while we fix  $\alpha_F = 70$  deg,  $\alpha_B = 45$  deg,  $a = 20$  mm,  $b = 25$  mm, and  $d = 10$  mm for all three variants. To analyze the behavior of this chain of Shrimp units, we consider each unit as a nonlinear one-dimensional spring, as shown in the left half of Fig. 9(a). This is referred to as the chain model in Fig. 9.

Owing to the additional kinematic constraints implicitly induced by neighbor units in the tessellation, we update the boundary conditions used in Sec. 4 by removing the support on vertex  $O_6$  as it seems to be over restrictive. The compatibility between adjacent units is enforced by requiring that the angular difference between  $\psi'$  of one unit and  $\psi''$  of the next unit to be less than  $0.01\pi$ . This chain tessellation has one zero energy phase and seven metastable phases. We consider a scenario when the whole chain is compressed by an amount of  $u_A = 2L_{R,AB}$ . Qualitatively, we expect that there are three possible metastable phases, encoded by (E,E,M), (E,M,E), and (M,E,E), as illustrated in the right part of Fig. 9(a). The three major DOFs of the system are given by  $u_A$ ,  $u_B$ , and  $u_C$ , as shown in Fig. 9(a). Based on the displacement–energy relationship revealed by numerical analysis of each individual unit, we can draw the

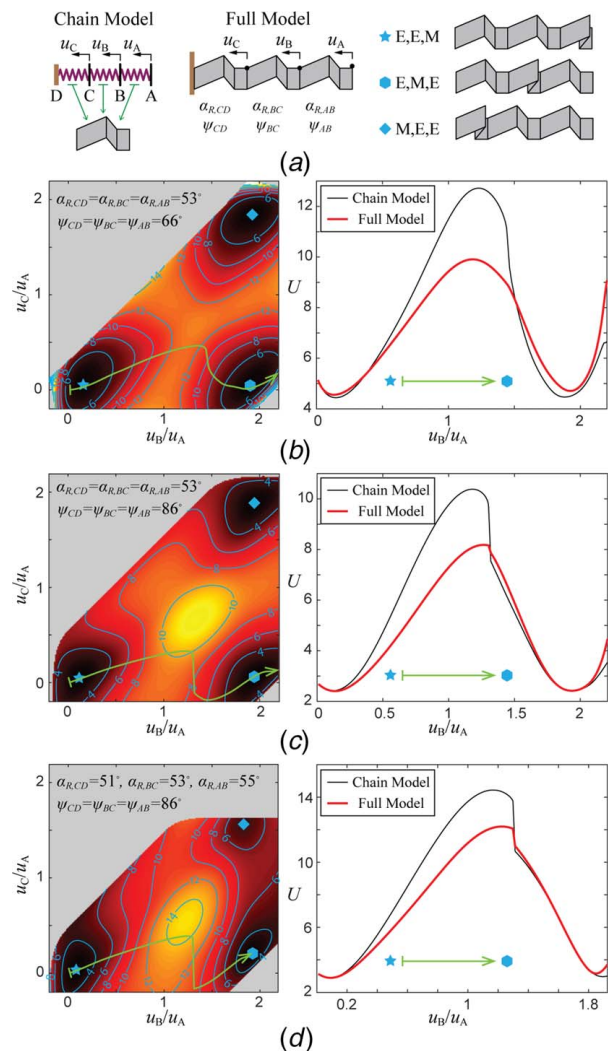


**Fig. 9 Energy landscape of a  $1 \times 3$  tessellation of Shrimp units when subject to a compression displacement load of  $u_A = 2L_{R,AB}$  at its end. The gray area are incompatible configurations judged by the condition that the angular difference between  $\psi'$  of one unit and  $\psi''$  of the next unit to be less than  $0.01\pi$ . (a) Illustration of the chain model and the full model. Sketches of the three metastable phases are shown on the right. (b) The energy landscape of variant (1) presented in contour plot. The plot on the right shows a comparison between the chain model prediction and the full model simulation along the same kinematic path for transitioning from one metastable phase to another, which is indicated by the solid line with arrow in the energy contour plot. (c) The energy contour plot and comparison between the chain model and the full model for variant (2). (d) The energy contour plot and comparison between the chain model and the full model for variant (3).**

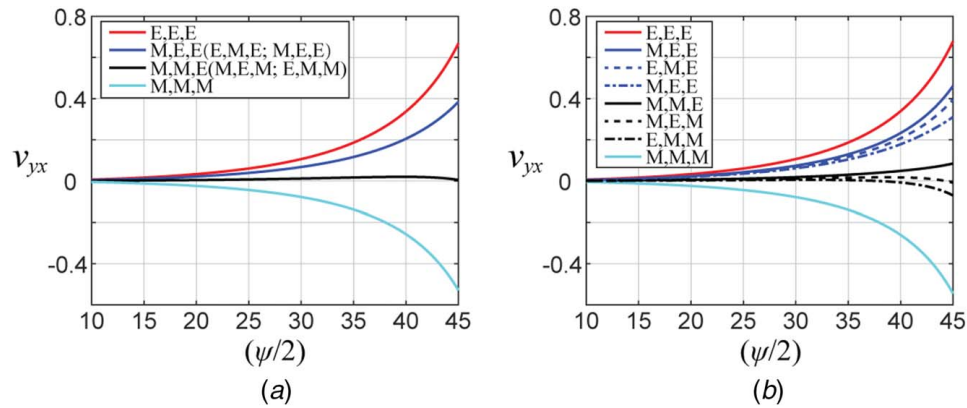


**Fig. 10 Property of the Shrimp tessellated material at different phases. (a) Poisson's ratio at different phases of variant (1). Note that some phases share the same property. (b) Poisson's ratio at different phases of variant (3). All phases have different properties.**

complete energy landscape of the tessellation to reveal its three metastable states, as shown in Figs. 9(b)–9(d) for the three different variants of the chain tessellation. We can see that when the three units are the same, as of variants (1) and (2), the energy landscape is symmetric. However, when the three units are different in geometry, the energy landscape becomes asymmetric, and the energy state associated with unit CD in its Miura mode has a higher energy compared to the other two metastable states. This is because unit CD has a smaller  $\alpha_R$ , as well as  $L_R$ , and hence at  $u_A = 2 L_{R,AB}$ , the whole chain needs to be further compressed beyond unit CD's metastable state, which causes the system to store extra elastic energy.

To verify the predictions made by the simplified chain model, we perform simulation on a full model considering all three units. We make sure that in the full model, each unit is subject to equivalent boundary conditions as in the single unit simulation. We first find the local equilibrium of the chain tessellation when unit AB is at its Miura mode. We compute an initial rigid origami configuration as unit AB in its Miura mode (configuration 2) and units BC and CD in their eggbox modes (configuration 2), which is approximately the geometry of the metastable state (E,E,M). However, the zero energy states of the folding angles are set to be the same as all three units in their eggbox mode. This leads to some unbalanced forces in the chain, which is then intermediately resolved at the first increment of the nonlinear structural analysis as the algorithm seeks for equilibrium at the end of each increment [28]. Next, a displacement load  $u_B$  is applied while  $u_A$  is fixed to transition the tessellation from metastable state (E,E,M) to (E,M,E). This simulation results in a path on the energy landscape from one local minimum to another, which is then compared with the chain model predictions, as shown on the right sides of Figs. 9(b)–9(d). We find that the chain model is quite accurate, especially near the metastable

states. Deviating from the stable states, the chain model appears to be stiffer than the full mode, because its DOFs are much less than the full model.

In each of the different phases, the Shrimp tessellated material displays different mechanical properties. Figure 10 shows how Poisson's effect behaves differently for the variant (1) at different phases. Moreover, as the three units are the same, some phases behave the same way. Therefore, we can only find four distinct branches on Poisson's ratio diagram. However, variant (3) has three different units, and hence its eight phases all behave differently, as shown in Fig. 10(b). Such a feature allows us to reprogram the material after it is manufactured, through mechanical phase transitions (i.e., snap-through), as illustrated in Fig. 11.

## 6 Concluding Remarks

The Shrimp origami pattern enables architected metamaterials with programmable metastable phases through mechanical phase transitions. The Shrimp pattern unit is created by modifying the geometry of a rigid foldable pattern to block a range of rigid folding kinematics, which can only be overcome by non-rigid origami deformation. The non-rigid deformation separates the rigid folding kinematics of a Shrimp pattern into two disconnected ranges. Thus, the programmable Shrimp pattern can display both rigid origami and non-rigid origami behavior. We study the connection between the geometry of a shrimp unit cell and its bistable behavior. An analytical estimation function is derived to approximate the energy barrier between the two stable states of a shrimp unit cell. The bistable Shrimp unit can be tessellated to form architected metamaterials. We show an example of the Shrimp tessellated materials with multiple stable configurations, which are interpreted as metastable phases. To transition from one phase to another, the tessellation must overcome an energy barrier through mechanical snapping. In each of the different phases, the metamaterial displays different mechanical properties, characterized here by Poisson's ratio (yet other properties can also be explored). In Appendix B, we discuss approaches to fabricate such non-developable patterns.

Future investigation includes conducting experiments on the Shrimp pattern to investigate the performance of samples provided by different manufacturing techniques. In addition, the 3D stacking of the Shrimp pattern should be explored towards applications as smart multi-phase cellular materials.

## Acknowledgment

We thank the support from the US National Science Foundation (NSF) through Grant No. 1538830, the Japan Science and Technology Agency (JST) PRESTO through Grant No. JPMJPR1927, and

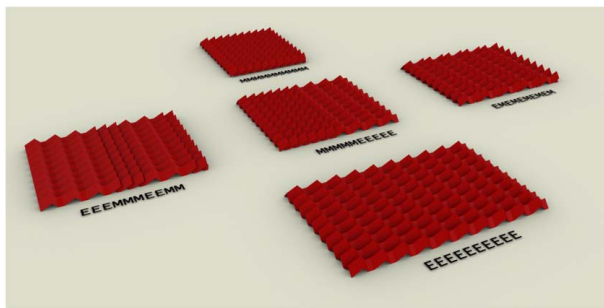


**Fig. 11 Examples of different metastable phases obtained from a single piece of Shrimp tessellated material. The text next to each configuration encodes its phase.**

the Raymond Allen Jones Chair at Georgia Tech. We are grateful to Emily D. Sanders for her helpful comments and suggestions to this paper.

### Conflict of Interest

There are no conflicts of interest.

### Data Availability Statement

The authors attest that all data for this study are included in the paper. Data provided by a third party are listed in Acknowledgements.

### Appendix A: Generalization of the Shrimp Pattern

Varying the geometry of the Shrimp pattern unit cell allows it to tessellate curved chains, such as the shrimp shape shown in Fig. 1. This is done by creating angular deficit on each of the shrimp units in an assemblage. Here, we illustrate the strategy by looking at the flat folded states of the Shrimp pattern, as shown in Fig. 12.

In the flat folded state of a standard Shrimp pattern unit cell (eggbox mode), the points  $O_5$  and  $O_8$  lie on a line parallel to the line passing through  $O_1$  and  $O_4$ . These two parallel lines can be regarded as concentric circles of infinite radius (Fig. 12(a)). When we generalize the radii of the two concentric circles from infinite to finite values, we can construct a Shrimp unit cell that leads to a curved tessellation. As shown in Fig. 12(b), in the generalized Shrimp pattern unit cell, the lines of  $O_1 O_5$ ,  $O_4 O_8$  are perpendicular to the circles passing through  $O_1 O_4$  and  $O_5 O_8$ , instead of the straight lines in the standard version. Now both lines of  $O_1 O_5$ ,

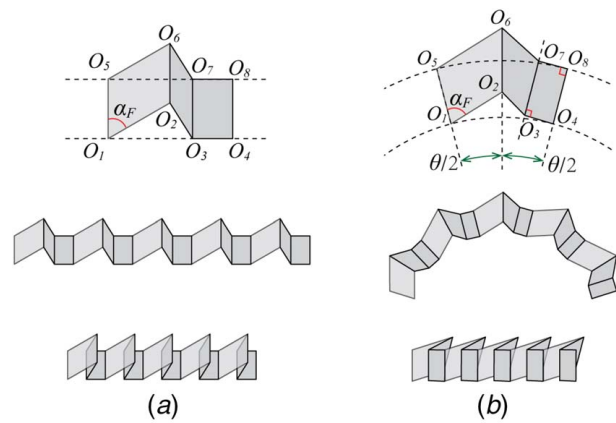


**Fig. 12** Geometry of a generalized shrimp unit cell for curved tessellation. (a) From top to bottom: the flat folded state of a standard Shrimp pattern unit cell in eggbox mode; the flat folded state of a 1D tessellation (eggbox mode); and the flat folded state of the 1D tessellation (Miura mode); (b) from top to bottom: the flat folded state of a generalized Shrimp pattern unit cell in eggbox mode; the flat folded state of a 1D tessellation (eggbox mode); and the flat folded state of the 1D tessellation (Miura mode).

$O_4 O_8$  are pointing to the shared center of the two circles. We let the extended line of  $O_2 O_6$  to pass through the center, and let this line to bisect the angle formed by lines of  $O_1 O_5$  and  $O_4 O_8$ . As in the standard version,  $O_1 O_2$  is parallel to  $O_5 O_6$ , while the panel angle  $\alpha_F$  is still a free design parameter. Following this design protocol, the front panel  $O_1 O_2 O_6 O_5$  becomes an obtuse

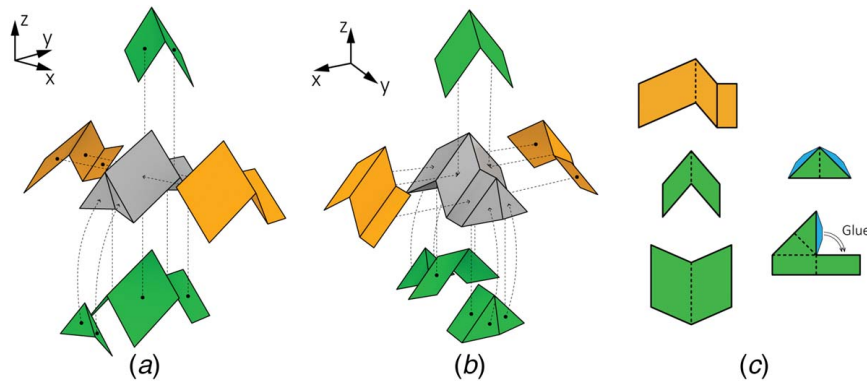


**Fig. 13** The double layer technique. We fabricate developable stripes and glue them in two directions to make the non-developable Shrimp pattern. We demonstrate the fabrication of a single unit cell in this figure. The correspondence of panels are shown in (a) and (b), from difference view angles. The designs of developable stripes are shown in (c). (d) A  $4 \times 4$  patch of Shrimp pattern made using the double layer technique. The sheet material we used is the 63lb premium ICE paper (Durilla Durable Papers, CTI Paper USA, WI).

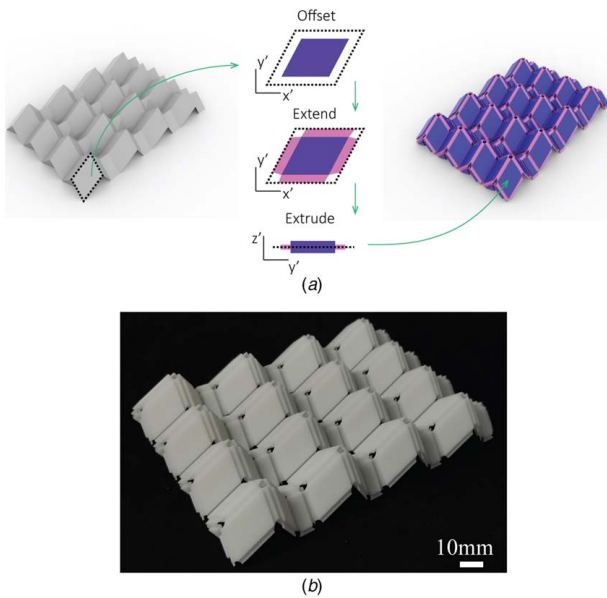


**Fig. 14 Shrimp pattern by 3D printing. (a) Procedure to prepare 3D printable solid from geometric data of a Shrimp origami surface. (b) A 3D printed Shrimp pattern using the selective laser sintering (SLS) technology. The sample shown in (b) is printed by SLS technology using a rubbery TPU material.**

trapezoid instead of a parallelogram. We also keep the rectangle shape of the tail panel  $O_3 O_4 O_8 O_7$ . As a result, the rear panel  $O_2 O_3 O_7 O_6$  becomes a general quadrilateral. The generalized Shrimp pattern unit cell forms an angular deficit  $\theta$ , such that a 1D tessellation leads to a curvature of  $\theta/L$ , where  $L = \|O_1 O_4\|$ . When all unit cells in a tessellation are folded flat into the Miura mode, the curvature disappears and the tessellation becomes straight, as shown in Fig. 12(b). The Miura mode flat folded state can be obtained from the eggbox mode by two reflections about  $O_2 O_6$  and  $O_3 O_7$ .

## Appendix B: Fabrication of the Shrimp Pattern

The Shrimp pattern contains non-developable vertices, thus it cannot be folded from a single piece of flat sheet, like the Miura-ori. We fabricate the Shrimp pattern by gluing thin sheets or 3D printing.

We adopt a double layer technique to glue stripes of thin sheets, which is demonstrated in Fig. 13. The advantage of this strategy is that we obtain uniform thickness over the panels (double layers) and creases (single layer). The creases are treated by perforation or etching to reduce its folding stiffness. As we can observe from Fig. 7, to enable bistability, the Shrimp pattern needs to have a large  $k_0^B/k_0^F$  ratio. By making the panels thicker, the double layer technique further increases the ratio of  $k_0^B/k_0^F$ .

Additive manufacturing technologies provide another avenue to realize the Shrimp pattern design. An automatic algorithm is written in Rhino/Grasshopper to generate a printable solid given an origami design. The printable solid is thicker within panels and thinner along folding hinges in order to differentiate their stiffness. The thin hinges and thick panels can also be printed with different materials. The procedure is outlined in Fig. 14.

## References

[1] Patek, S. N., Nowroozi, B. N., Baio, J. E., Caldwell, R. L., and Summers, A. P., 2007, "Linkage Mechanics and Power Amplification of the Mantis Shrimp's Strike," *J. Exp. Biol.*, **210**, pp. 3677–3688.  
 [2] Patek, S. N., 2015, "The Most Powerful Movements in Biology," *Am. Sci.*, **103**(5), pp. 330–337.

[3] Forterre, Y., Skotheim, J. M., Dumais, J., and Mahadevan, L., 2005, "How the Venus Flytrap Snaps," *Nature*, **433**, pp. 421–425.  
 [4] Saito, K., Nomura, S., Yamamoto, S., Niiyama, R., and Okabe, Y., 2017, "Investigation of Hindwing Folding in Ladybird Beetles by Artificial Elytron Transplantation and Microcomputed Tomography," *Proc. Natl. Acad. Sci. USA*, **114**(22), pp. 5624–5628.  
 [5] Faber, J. A., Arrieta, A. F., and Studart, A. R., 2018, "Bioinspired Spring Origami," *Science*, **359**(6382), pp. 1386–1391.  
 [6] Florijn, B., Coullais, C., and van Hecke, M., 2014, "Programmable Mechanical Metamaterials," *Phys. Rev. Lett.*, **113**(17), p. 175503.  
 [7] Bertoldi, K., Vitelli, V., Christensen, J., and van Hecke, M., 2017, "Self-Folding Origami at Any Energy Scale," *Nat. Rev. Mater.*, **2**, p. 17066.  
 [8] Kang, S. H., Shan, S., Noorduyn, W. L., Khan, M., Aizenberg, J., and Bertoldi, K., 2013, "Buckling-Induced Reversible Symmetry Breaking and Amplification of Chirality Using Supported Cellular Structures," *Adv. Mater.*, **25**(24), pp. 3380–3385.  
 [9] Liu, J., and Zhang, Y., 2018, "Soft Network Materials With Isotropic Negative Poisson's Ratios Over Large Strains," *Soft Matter*, **14**(5), pp. 693–703.  
 [10] Shan, S., Kang, S. H., Raney, J. R., Wang, P., Fang, L., Candido, F., Lewis, J. A., and Bertoldi, K., 2015, "Multistable Architected Materials for Trapping Elastic Strain Energy," *Adv. Mater.*, **27**(29), pp. 4296–4301.  
 [11] Tan, X., Chen, S., Wang, B., Zhu, S., Wu, L., and Sun, Y., 2019, "Design, Fabrication, and Characterization of Multistable Mechanical Metamaterials for Trapping Energy," *Extreme Mech. Lett.*, **28**, pp. 8–21.  
 [12] Mullin, T., Deschanel, S., Bertoldi, K., and Boyce, M. C., 2007, "Pattern Transformation Triggered by Deformation," *Phys. Rev. Lett.*, **99**(8), p. 084301.  
 [13] Shang, X., Liu, L., Rafsanjani, A., and Pasini, D., 2018, "Durable Bistable Auxetics Made of Rigid Solids," *J. Mater. Res.*, **33**(3), pp. 300–308.  
 [14] Jin, L., Khajetourian, R., Mueller, J., Rafsanjani, A., Tournat, V., Bertoldi, K., and Kochmann, D. M., 2020, "Guided Transition Waves in Multistable Mechanical Metamaterials," *Proc. Natl. Acad. Sci. USA*, **117**(5), pp. 2319–2325.  
 [15] Che, K., Yuan, C., Wu, J., Qi, H. J., and Meaud, J., 2017, "3D-Printed Multistable Mechanical Metamaterials With a Deterministic Deformation Sequence," *ASME J. Appl. Mech.*, **84**(1), p. 011004.  
 [16] Haghpanah, B., Salari-Sharif, L., Pourrajab, P., Hopkins, J., and Valdevit, L., 2016, "Multistable Shape-Reconfigurable Architected Materials," *Adv. Mater.*, **28**(36), pp. 7915–7920.  
 [17] Yang, D., Jin, L., Martinez, R. V., Bertoldi, K., Whitesides, G. M., and Suo, Z., 2016, "Phase-Transforming and Switchable Metamaterials," *Extreme Mech. Lett.*, **6**, pp. 1–9.  
 [18] Zhai, Z., Wang, Y., and Jiang, H., 2018, "Origami-Inspired, On-Demand Deployable and Collapsible Mechanical Metamaterials With Tunable Stiffness," *Proc. Natl. Acad. Sci. USA*, **115**(9), pp. 2032–2037.  
 [19] Silverberg, J. L., Evans, A. A., McLeod, L., Hayward, R. C., Hull, T., Santangelo, C. D., and Cohen, I., 2014, "Using Origami Design Principles to Fold Reprogrammable Mechanical Metamaterials," *Science*, **345**(6197), pp. 647–650.  
 [20] Pinson, M. B., Stern, M., Ferrero, A. C., Witten, T. A., Chen, E., and Murugan, A., 2017, "Self-Folding Origami At any Energy Scale," *Nat. Commun.*, **8**, p. 15477.  
 [21] Iniguez-Rabago, A., Li, Y., and Overvelde, J. T. B., 2019, "Exploring Multistability in Prismatic Metamaterials Through Local Actuation," *Nat. Commun.*, **10**, p. 5577.  
 [22] Zhai, Z., Wang, Y., Lin, K., Wu, L., and Jiang, H., 2020, "In Situ Stiffness Manipulation Using Elegant Curved Origami," *Sci. Adv.*, **6**(47), p. eabe2000.  
 [23] Mukhopadhyay, T., Ma, J., Feng, H., Hou, D., Gattas, J. M., Chen, Y., and You, Z., 2020, "Programmable Stiffness and Shape Modulation in Origami Materials: Emergence of a Distant Actuation Feature," *Appl. Mater. Today*, **19**, p. 100537.  
 [24] Silverberg, J. L., Na, J. H., Evans, A. A., Liu, B., Hull, T., Santangelo, C. D., Lang, R. J., Hayward, R. C., and Cohen, I., 2015, "Origami Structures With a Critical Transition to Bistability Arising From Hidden Degrees of Freedom," *Nat. Mater.*, **14**, pp. 389–393.  
 [25] Yasuda, H., Tachi, T., Lee, M., and Yang, J., 2017, "Origami-Based Tunable Truss Structures for No-Volatile Mechanical Memory Operation," *Nat. Commun.*, **8**, p. 962.  
 [26] Liu, K., and Paulino, G. H., 2019, "Invariant and Smooth Limit of Discrete Geometry Folded From Bistable Origami Leading to Multistable Metasurfaces," *Nat. Commun.*, **10**, p. 4238.  
 [27] Tachi, T., 2006, "Simulation of Rigid Origami," *Origami 4*, 1st ed., R. J. Lang, ed., A K Peters/CRC Press, Natick, MA, pp. 175–187.  
 [28] Liu, K., and Paulino, G. H., 2017, "Nonlinear Mechanics of Non-Rigid Origami: An Efficient Computational Approach," *Proc. R. Soc. A*, **473**(2206), p. 20170348.  
 [29] Pratapa, P., Liu, K., and Paulino, G. H., 2019, "Geometric Mechanics of Origami Patterns Exhibiting Poisson's Ratio Switch by Breaking Mountain and Valley Assignment," *Phys. Rev. Lett.*, **122**(15), p. 155501.  
 [30] Liu, B., Silverberg, J. L., Evans, A. A., Santangelo, C. D., Lang, R. J., Hull, T. C., and Cohen, I., 2018, "Topological Kinematics of Origami Metamaterials," *Nat. Phys.*, **14**, pp. 811–815.  
 [31] Filipov, E. T., Liu, K., Tachi, T., Schenk, M., and Paulino, G. H., 2017, "Bar and Hinge Models for Scalable Analysis of Origami," *Int. J. Solids Struct.*, **124**, pp. 26–45.  
 [32] Liu, K., and Paulino, G. H., 2018, "Highly Efficient Nonlinear Structural Analysis of Origami Assemblages Using the MERLIN2 Software," *Origami 7*, 1, Vol. 4, R. J. Lang, M. Bolitho, and Z. You, eds., Tarquin, Hertfordshire, UK, pp. 1167–1182.